



Effect of thermal treatment on the structural, electrical, and dielectric properties of volcanic scoria

Shoroog Alraddadi¹ · Abdu Saeed^{2,3} · Hasan Assaedi⁴

Received: 13 April 2020 / Accepted: 2 June 2020 / Published online: 6 June 2020
© Springer Science+Business Media, LLC, part of Springer Nature 2020

Abstract

The effects of thermal treatment on the structural, electrical, and dielectric properties of scoria collected from Harrat Rahat in Saudi Arabia have been investigated. The raw scoria was thermally treated at two different temperatures (800 and 1000 °C). The crystalline phase, morphology, and chemical group functions of natural and treated scoria samples were studied using XRD, SEM, FTIR/Raman spectroscopies, respectively. The XRD results showed no apparent differences between the raw sample and treated at the temperature of 800 °C. While it showed a decrease in the intensities of the XRD pattern and Raman spectra of the scoria treated at the temperature of 1000 °C, this could be attributed to the formation of a hematite–ilmenite solid solution. The tested raw scoria showed excellent thermal stability up to the temperature of 800 °C. At higher temperatures, however, its mineral and chemical compositions can be slightly affected. Electrical and dielectric properties were explored in detail at different temperatures and frequencies. The results did not show any considerable changes between raw and treated scoria samples. Likewise, conductivities and dielectric constants revealed stable values up to 700 K. This type of scoria, therefore, can be a promising material for use as high-voltage power insulators.

1 Introduction

Volcanic ashes are non-generic expressions that represent the fine crumbs of pyroclastic materials [1]. Regular volcanic ashes are pyroclastic wreckages, which are less than 2 mm [2]. They have fairly low reactivity in general; however, they have variable chemical, mineralogical, and physical properties [3]. Their physicochemical properties can play a crucial role in the assessment of their technological applications [4]. Volcanic ashes consist of many oxides; some oxides can be found as major components such as Al₂O₃, SiO₂, Fe₂O₃, CaO, MgO, Na₂O, and K₂O in addition to other oxides in minor percentages [5–7]. The minerals of the volcanic ashes grow within the magma under the earth's

surface. Therefore, the mineralogical compositions depend on both the eruption conditions and magma chemistry [1, 4]. They have widely varying physical properties such as structural, thermal, and optical properties. They have different degrees of crystallinities and vary from entirely amorphous to almost crystalline material [1, 4]. Based on their chemical and mineral compositions, their color can vary from black to poorly red [8].

Many of the volcanic ashes have been used as ceramic materials [4, 9], cement and concrete [10, 11], and geopolymer materials [3]. Many studies showed that the volcanic ashes in Saudi Arabia are excellent supplementary cementitious materials for about 30% replacement of ordinary Portland cement [10–12]. These volcanic ashes were produced by active volcanoes in the region of the Arabian Gulf; therefore, there are abundances of volcanic materials that could be used in many applications [12], which could be an economical source.

Scoria is one of the volcanic ashes that commonly used in applications due to its morphology and microstructure [8, 13–15]. Scoria has been utilized for hundreds of years in worldwide as a building material [16]. Many researchers investigated the effect of scoria as alternative materials for cement [17, 18], thermal activation [19], and the fabrication of lightweight concrete [20]. It was reported that

✉ Hasan Assaedi
hsassaedi@uqu.edu.sa

¹ Department of Physics, Umm Al-Qura University, Makkah 24382, Saudi Arabia

² Department of Physics, Faculty of Science, King Abdulaziz University, Jeddah 21589, Saudi Arabia

³ Department of Physics, Tamar University, Tamar, Yemen

⁴ Department of Physics, University College in AlJumum, Umm Al-Qura University, Makkah 21955, Saudi Arabia

scoria could act as a friendly, economical, and ecological building material [21]. It has promising applications, and there is a global abundance of different unexploited sediments [10–13]. Nevertheless, the studies and research on the volcanic ash generally and scoria particularly are still limited in comparison to the fly ash that has been subjected to many studies [22–27].

To the best of our knowledge, the effect of heat treatments on structural, electrical conductivity, dielectric constant, and dielectric loss of scoria has not been studied yet. Therefore, this work aimed to investigate the effect of heat treatment on the structural, electrical, and dielectric properties of scoria. For this purpose, the thermal properties of raw scoria were explored using thermogravimetric analysis as well as differential scanning calorimetry analysis (TGA–DSC). According to the thermal results, the raw scoria was thermally treated at different temperatures. The structural phases and morphological features were investigated by X-ray diffraction (XRD) and scanning electron microscopy (SEM), respectively, while the mineralogical characterizations were studied using X-ray fluorescence spectrometry (XRF). In addition, chemical functional groups were explored using Raman/Fourier-transform infrared (FTIR) spectroscopy. The electrical and dielectric properties of raw and treated scoria were investigated at temperature range up to 1100 K at different frequencies range, starting from 500 Hz up to 4 MHz.

2 Materials and methods

2.1 Collection and processing the samples

The samples of scoria were collected from Harrat Rahat located in the western region of Saudi Arabia. Harrat Rahat is a fertile region with numerous pyroclastic scoria [28–30]. The raw material of scoria has particle sizes ranging between 0.01 and 32 mm and poor red color. The sample was ground to normal powder using a crusher unit, then smoothed using a smoothing machine Pulverizers agate (ROCKLABS, New Zealand) to attain a fine powder. The thermal properties were investigated in static air to estimate the heat treatment temperatures of scoria. The thermal measurement was performed with a heating rate of 5 °C/min at the temperature range starting from room temperature up to 1300 °C using TGA–DSC (NETZSCH, Germany). According to the thermal analysis results, three samples of scoria were tested; one was as raw, and the other two were thermally treated in a muffle furnace at temperatures of 800 and 1000 °C with a heating rate of 5 °C/min for 1 h. Finally, the samples were named as Raw, 800, and 1000.

2.2 Characterization techniques

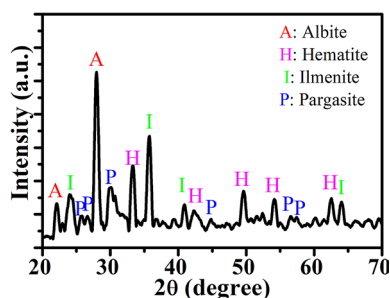
The chemical analyses of the samples were carried out using XRF with SPECTRO XEPOS (AMETEK Inc., USA) to determine the oxides elements (wt%). For XRF analysis, Lithium Borate (0.5% LiBr, 32.83% LiBO₂, and 66.67% Li₂B₄O₇) is required as most oxides are best dissolved in lithium borate salts. One gram of scoria powder was added in the platinum crucible and mixed homogenously with 8 g of Lithium Borate then transferred to the fusion system for 20 min till the mixture converted to glass disk. The crystalline phases were determined by XRD with a Bruker D8 Advance XRD (Bruker, USA), Cu K α Ni-filtered radiation with a wavelength of 1.54 Å. The samples were scanned in an angular range (2θ) from 20° to 70°. Cards of the International Centre for Diffraction Data (ICDD) were utilized to identify the phases of the samples. The morphologies of the samples were scanned by SEM model JEOL 7600f (JEOL, Japan). The FTIR spectra of the samples were recorded using Nicolet (iS50 FTIR) FTIR spectrometer (Thermo Fisher Scientific, USA). Raman spectra of the scoria samples were recorded by Micro Raman microscope model DXR (Thermo Fisher Scientific, USA) equipped with diode-pumped solid-state (DPSS) laser 532 nm for sample's excitation. Raman system has a high-precision motorized stage in X and Y dimensions with a software-controlled Z focus. A 50X objective was used to collect the back-scattered radiation at 10 mW excitation laser power.

2.3 Electrical and dielectric measurements

The scoria samples were prepared as pellets to measure electrical and dielectric properties. Pellets were fabricated using a manual hydraulic press with a diameter and thickness of 13 and 2 mm, respectively. For fabrication of the pellets, the powders of the samples were mixed with 3.5 wt% of polyvinyl alcohol (PVA) as a binder. More details about the fabrication procedure can be found in the published works [31–33]. The pellets were heated at 800 °C for 2 h in air atmosphere. Both two faces of the pellets were polished to make perfect electrical contact. Then, they were coated by a high-performance silver paste (TED PELLA INC, USA) to form electrodes. After that, the pellets of the scoria samples were dried at 150 °C for 1 h. HIOKI LCR bridge as an impedance analyzer model Hioki 3532-50 LCR Hi-Tester (Hioki, Japan) was utilized to carry out the ac electrical and dielectric measurements. The measurements were performed using constant voltage (CV) mode at different frequencies starting from 500 Hz up to 4 MHz, and temperatures range up to 1100 K, with a heating rate of 2 °C/min. Through an RS-232C serial

Table 1 Chemical compositions (wt.%) of the collected raw scoria used in this study

Elements	SiO ₂	Al ₂ O ₃	CaO	Fe ₂ O ₃	K ₂ O	MgO	MnO	Na ₂ O	P ₂ O ₅	TiO ₂	SO ₃	L.O.I
wt%	44.89	15.25	8.63	14.16	0.71	6.33	0.19	4.26	0.55	3.09	<0.05	0.85

**Fig. 1** XRD pattern of raw scoria obtained from Harrat Rahat in the western region of Saudi Arabia

port, the measurements were taken digitally at a regular temperature step of 10 °C.

3 Results and discussion

3.1 Structural properties

The chemical compositions of the raw scoria were determined by XRF for both major and minor elements (expressed as % oxides). The raw scoria contains SiO₂, Al₂O₃, CaO, and Fe₂O₃ as major elements and K₂O, MgO, MnO, Na₂O, P₂O₅, TiO₂, and SO₃ as minor elements (Table 1).

The structural and mineral properties of raw scoria were investigated using XRD. Figure 1 shows the XRD pattern of raw scoria that was obtained from Harrat Rahat in the western region of Saudi Arabia. As can be seen, the XRD pattern of raw scoria indicates the presence of a high degree of crystallinity and exhibits different peaks with 2θ in the range between 20° and 70° that is characteristic of various minerals present in raw scoria. Based on the literature [34–38] and ICCD cards No; 00-001-1053, 01-070-6267, 00-003-0451, and 00-023-1406, four phases were found, and referred to albite (NaAlSi₃O₈), pargasite (NaCa₂Mg₄Al₃Si₆O₂₂(OH)₂),

hematite (α-Fe₂O₃), and ilmenite (FeTiO₃). These phases were indexed to their peaks, as shown in Fig. 1. The major minerals composition of scoria is albite and pargasite, and the minor minerals are ilmenite and hematite. Albite, pargasite, and hematite are insulators, while ilmenite is a conductive mineral [39, 40]. The structural refinements and mineral quantifications of raw scoria were carried out by applying the Rietveld analysis to the XRD pattern. The diffraction peaks were shaped using a B-spline function. The space group and lattice parameters of every phase were calculated and found in good agreements with PDF files. Using whole powder pattern fitting (WPPF) and based on the full width at half maximum (FWHM), the mean crystallite sizes were calculated using Scherrer's equation:

$$D = \frac{0.94\lambda}{\beta_{1/2} \cos \theta} \quad (1)$$

where $\beta_{1/2}$ is FWHM of the diffraction band, θ is the angle of diffraction, D is the crystalline size, and λ is the X-ray wavelength. The weighted percentages of crystalline phases were calculated only from the crystalline content of the sample. The results obtained by XRD analysis are listed in Table 2.

The thermal treatment is an important factor. It leads to many structural transformations such as decomposition, oxidation, hydroxyl migration, hydroxylation, surface reconstruction, and formation of new phases [41–44]. Therefore, thermal analyses were conducted on the powder of raw scoria. Figure 2 shows TGA–DSC curves that were recorded in static air with a heating rate of 5 °C/min. It is obvious from TGA that the scoria is almost thermally stable up to 1300 °C, with a weight loss of about 1.5%. The loss in the weight could be attributed to the trapped gases that release and come out of scoria particles during thermal heating. DSC exhibited a strong endothermic peak at a temperature of 1200 °C. It could be attributed to densification–vitrification with fusion and structural breakdown of scoria mineral

Table 2 Mineral phases present in scoria with their quantifications, lattice parameters, crystallite sizes, and space groups obtained by XRD analysis

Phase name	Formula	Lattice parameters			Crystallite size (Å)	Space group	Weighed (%)
		a (Å)	b (Å)	c (Å)			
Hematite	α-Fe ₂ O ₃	5.037	5.037	13.704	97.1	R-3c, hexagonal	15.5
Ilmenite	FeTiO ₃	5.081	5.081	14.169	119.9	R-3, hexagonal	6.9
Albite	NaAlSi ₃ O ₈	8.115	12.924	7.2132	120.1	P-1	40.1
Pargasite	NaCa ₂ Mg ₄ Al ₃ Si ₆ O ₂₂ (OH) ₂	9.892	18.046	5.3112	71.2	C12/m1, unique-b, cell-1	37.5

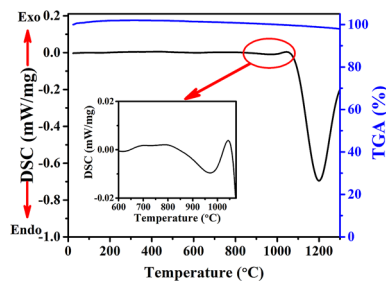


Fig. 2 Thermal analysis of the raw scoria powder (black line) DSC curve and (blue line) TGA. The inset shows the endothermic peak at 966 °C

compositions [9, 44]. From DSC analysis, scoria seemed to be thermally stable up to 1000 °C. However, there is a very weak endothermic peak at around 966 °C with an onset temperature of 820 °C, the expansion of this peak is shown in the inset of Fig. 2. From the mineral compositions obtained by XRD for raw scoria, hematite and ilmenite are two mineral phases, which can form a solid solution [45, 46]. Therefore, this weak endothermic peak could be attributed to the formation of the solid solution of (hematite–ilmenite).

According to the thermal analysis results, two samples of raw scoria were then thermally treated at temperatures of 800 °C and 1000 °C in static air. Therefore, three samples of scoria (Raw, 800, and 1000 scoria samples) will then be studied by XRD, SEM, and FTIR/Raman spectroscopies. In addition, their electrical and dielectric properties will be investigated.

Figure 3 shows XRD patterns of Raw, 800, and 1000 scoria samples. The XRD pattern for the powder of sample 800 was found to be identical to the Raw sample with no change in the peak positions, peak intensities, or crystal structure. The only eminent variation is the XRD pattern for the powder of sample 1000 exhibited a significant decrease in the all XRD peaks intensities with no change in the peak positions or crystal structure. The crystallite sizes were found to be somewhat increased with increasing the

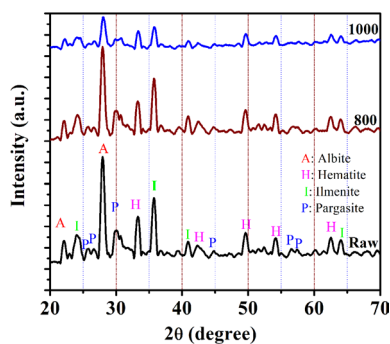


Fig. 3 XRD patterns of Raw, 800, and 1000 scoria samples

Table 3 Crystallite sizes of mineral phases present in Raw, 800 and 1000 scoria samples

Phase name	Formula	Crystallite size (Å)		
		Raw	800	1000
Hematite	$\alpha\text{-Fe}_2\text{O}_3$	97.1	100.2	115.6
Ilmenite	FeTiO_3	119.9	121.5	123.4
Albite	$\text{NaAlSi}_3\text{O}_8$	120.1	122.7	123.3
Pargasite	$\text{NaCa}_2\text{Mg}_4\text{Al}_3\text{Si}_6\text{O}_{22}(\text{OH})_2$	71.2	76.4	86.2

thermal temperature. The calculated mean crystallite sizes for all samples are listed in Table 3. The reduction in the XRD patterns at sample 1000 could be most likely due to the effect of trapped gases, which come out from the lattice and could have generated defects in the lattice, or from the impurities that might happen because of interference between the atoms of mineral phases (i.e., hematite, ilmenite, albite, and pargasite), which drive the impurities in each phase. Besides, the dissolution of crystalline phases could happen due to the high temperature (1000 °C).

Figure 4a–d displays SEM micrographs of raw scoria before grinding, raw scoria after grinding, 800, and 1000, respectively. As can be seen in Fig. 4a, morphological properties of raw scoria sample before grinding showed no specific shapes; it exhibited numerous particles with huge aggregate and mixture of nano/microsized, which intercalated with each other to form bulk scoria. Raw scoria sample after grinding showed similar morphologies only with small aggregate and some fragments with nanosized (Fig. 4b), which resulted from the grinding process. Sample 800 that was thermally treated at a temperature of 800 °C showed that the particles and fragments started to accumulate again (Fig. 4c), while the 1000 sample that was treated at temperatures of 1000 °C exhibited a dense matrix without clear particles' boundaries (Fig. 4d). This can be understood from the formation of (hematite–ilmenite) solid solution that could weld between particles of all mineral compositions.

Figure 5 displays the FTIR analysis of Raw, 800, and 1000 scoria samples. A broad and intense absorption peak in the range between 1250 and 800 cm^{-1} can be noticed in all samples, this peak centered at 996 cm^{-1} . In addition, two shoulder peaks can be distinguished at 1125 and 1025 cm^{-1} . These peak and shoulder peaks were attributed to the asymmetric stretching vibration of Si–O–T (T: Si or Al) bonds [6, 7, 43, 47–49] in the mineral phases of albite and pargasite. FTIR spectra for all scoria samples exhibited nearly the same peaks without significant shifting (Fig. 5). The intensities of peaks in the FTIR spectrum of sample 1000 get decreased comparing with Raw and 800 scoria samples, this is the only difference between the FTIR spectra of scoria samples. This decrease may result from the change in the

Fig. 4 Scoria SEM images of **a** Raw before grinding **b** Raw after grinding **c** 800 **d** 1000

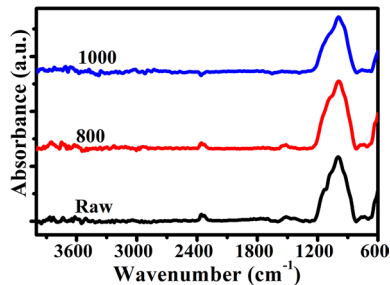
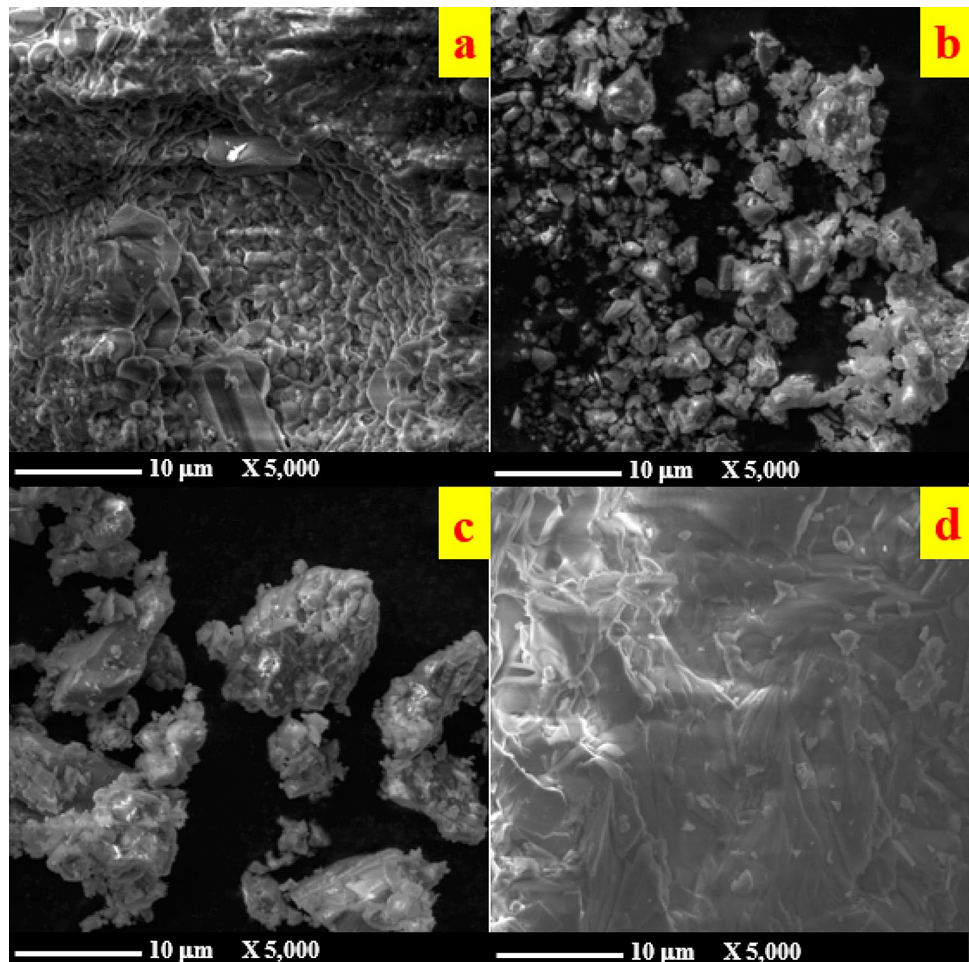


Fig. 5 FTIR spectra of Raw, 800, and 1000 scoria samples

structure of Si–O–T (T: Si or Al), where heat treatment and formation of (hematite–ilmenite) solid solution affected the molecular structure of mineral phases albite and pargasite. FTIR results are in good agreement with that obtained by XRD.

Raman spectra of Raw, 800, and 1000 scoria samples are shown in Fig. 6. As can be seen, Raman spectra exhibit different peaks. The strongest peak centered at 1321 cm^{-1} characterizes the hematite mineral phase [50, 51], the peak located at 672 cm^{-1} was attributed to the ilmenite and

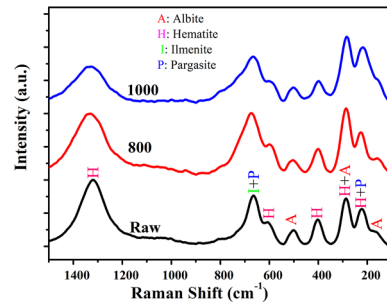


Fig. 6 Raman spectra of Raw, 800, and 1000 scoria samples

pargasite mineral phases [51, 52], while the shoulder peak situated at around 602 cm^{-1} was referred to as the hematite mineral phase [50, 51]. The peak in the range between 540 and 460 cm^{-1} referred to albite mineral phase [53, 54], the peak centered at 402 cm^{-1} was attributed to the hematite mineral phase [50, 51], while the peaks centered at 288 and 223 cm^{-1} were attributed to hematite/albite [50, 51, 54] and hematite/pargasite mineral phases [51], respectively. Finally, the shoulder peak at 161 cm^{-1} was referred to albite mineral

phase [53, 54]. As can be seen in Fig. 6, all tested samples have the same peaks nearly without significant shifting; the reduction in the intensities of the Raman peaks of the 1000 sample is the only noticeable difference comparing with the Raw and 800 scoria samples. This result is in a full agreement with those obtained by XRD and FTIR. It can be noticed the peaks that belong to either hematite or ilmenite get decreased more comparing with the peaks that belong only to either albite or pargasite.

3.2 Electrical and dielectric properties

The electrical and dielectric properties of Earth’s materials such as scoria is affected by several factors, including (i) the major element composition (mineral phases), (ii) temperature, (iii) porosity, (iv) grain boundaries, (v) impurities, (vi) the water content and the degree of partial melting. Alternating current conductivity (σ_{ac}) of Raw, 800, and 1000 scoria samples were investigated in temperatures starting from room temperature up to 1100 K at frequencies of 500 Hz, 1 kHz, 2 kHz, 5 kHz, 10 kHz, 20 kHz, 50 kHz, 100 kHz, 200 kHz, 500 kHz, 1 MHz, 2 MHz, and 4 MHz. The ac conductance (G) of every sample pellet was measured; then, σ_{ac} was calculated using the following relations [55, 56]:

$$\sigma_{ac} = G \frac{d}{A} \tag{2}$$

where d and A are the thickness and the cross-sectional area of sample, respectively. Figure 7 shows the $\ln \sigma_{ac}$ as a function of $1000/T$ at different applied frequencies for all scoria samples. As can be seen in this figure, all scoria samples (Raw, 800, and 1000 samples) showed nearly the same electrical behavior. Two distinct regions can be identified in the

conductivity spectra of scoria. The first region seems to be stable in which the electrical conductivity is almost without any changes. The scoria samples showed stable low electrical conductivities, although the temperatures were raised to nearly 700 K, so it can be said they were electrically insulators. Scoria is composed mostly of silicate minerals (albite, pargasite), which are essentially insulators, with a minor of ilmenite and hematite minerals. Therefore, the samples were of low electrical conductivity. This can take place when thermal energies are not enough to activate the hopping of carriers and ions [33]. The second region is at a higher temperature range, and this region started from a temperature of 700 K till 1100 K. The electrical conductivities in this region increased linearly with temperature.

As a rule, the increase in the electrical conductivity with increasing temperature pointed out the semiconducting properties of the material [57]. Therefore, at higher temperatures, all scoria samples showed semiconductor behaviors. This can be understood from that the thermal energies at higher temperatures become enough to induce more defects of oxygen vacancies [58, 59], which drive to increase the electrical conductivities. Subsequently, the conductivities are dominated by the process of thermal activation [60, 61]. Figure 8 shows the curves of the $\ln \sigma_{ac}$ as a function of applied frequency at different temperatures for Raw, 800, and 1000 scoria samples that exhibited gradual increases with frequencies at low temperatures. Thus, the conductivities of all scoria samples seem to be frequency-dependent, suggesting that the mechanism of conduction could happen through hopping of the charge carriers at lower temperatures [62–64]. Here, the frequency works as a force that eases the charge carriers to transfer between different localized states and liberate the trapped charges from their trapping centers [32]. However,

Fig. 7 Electric conductivity of Raw, 800, and 1000 scoria samples, $\ln \sigma_{ac}$ versus reciprocal of absolute temperature at different applied frequencies

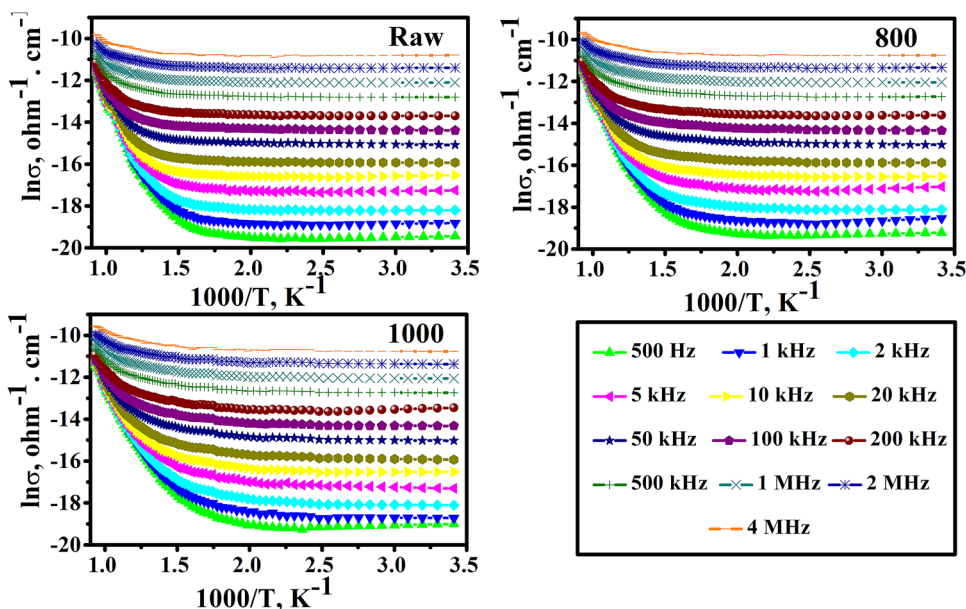
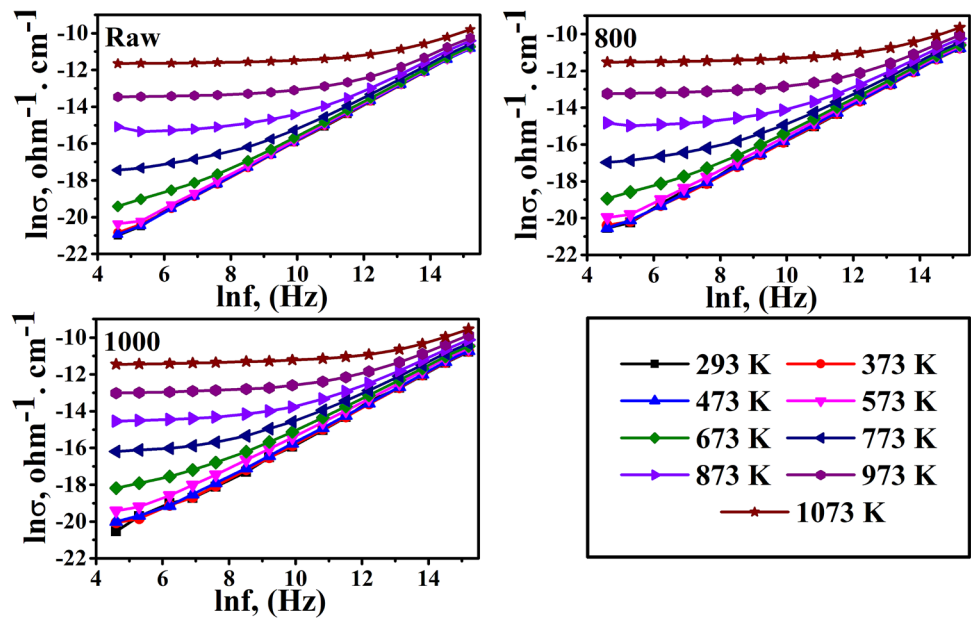


Fig. 8 $\ln \sigma_{ac}$ as a function of applied frequency at different temperatures for Raw, 800, and 1000 scoria samples



at a higher temperature region, the curves of the $\ln \sigma_{ac}$ are linear. Thus, the conductivities of all scoria samples seem to be frequency-independent, where the large vibrations of the lattice can scatter the charge carriers and abolish the effect of frequency [32]. The clear frequency independence at higher temperatures suggests that the mechanism of conduction becomes polarons conduction [62].

The polarization of any materials is shared out by four different polarization mechanisms viz. electronic polarization, ionic polarization, space charge polarization, and orientation polarization [65]. The complex dielectric permittivity (ϵ^*) of the materials is suitable for understanding the polarization of materials. The complex dielectric permittivity is given by the relation [60, 66, 67]

$$\epsilon^* = \epsilon' - j\epsilon'' \quad (3)$$

where the real part (ϵ') and the imaginary part (ϵ'') of the complex dielectric permittivity are called dielectric constant and dielectric loss, respectively. The dielectric constant points out the storage of energy or the polarizing ability of the material, whereas the dielectric loss points out the loss of energy in a material. The ratio between dielectric constant and dielectric loss is called dielectric loss tangent, $\tan \delta = \epsilon''/\epsilon'$. Both dielectric constant and dielectric loss can be, respectively, calculated by the following equations [65, 67, 68]:

$$\epsilon' = \frac{Cd}{\epsilon_0 A} \quad (4)$$

$$\epsilon'' = \epsilon' \tan \delta \quad (5)$$

where ϵ_0 is the free space permittivity, and C is the measured capacitance of the sample. Figures 9 and 10 display the dielectric constant and dielectric loss, respectively, versus absolute temperatures at different applied frequencies for Raw, 800, and 1000 scoria samples. It can be seen two behaviors, the first behavior started from room temperature up nearly to 700 K in which the curves of the dielectric constant and dielectric loss showed no alterations with changes the temperature at all applied frequencies. In this range of temperature, dielectric constant and dielectric loss appeared to be temperature-independent and frequency-independent. This points out that the dielectric properties of scoria samples have excellent thermal stability in these temperature and frequency ranges. The second behavior started from 700 up to 1100 K in which the curves of the dielectric constant and dielectric loss increased, particularly at low frequencies. In this region, the dielectric constant and dielectric loss seemed to be temperature-dependent; however, they decreased as the frequencies increased. The dielectric constants and dielectric loss appeared to be lower at lower temperatures suggesting the contribution of electronic and ionic components to all polarizabilities could be constant and small at lower temperatures [69]. However, at higher temperatures and lower frequencies, the rise of dielectric constant, suggesting the orientation of dipoles, might become easier [57, 69]. In addition, the increase in the temperature seems to be a pumping force that can liberate the trapped charge carriers and subsequently increase the polarization [57]. However, at higher temperatures, the decrease of dielectric constant with increases the frequencies indicating all the dipoles could not follow well the fast-applied field (higher frequencies) to reorient themselves quickly that finally leads to reduce the dielectric constants [33, 62]. As can be seen in Fig. 9, the

Fig. 9 Dielectric constant (ϵ') as a function of absolute temperature at different applied frequencies for Raw, 800, and 1000 scoria samples

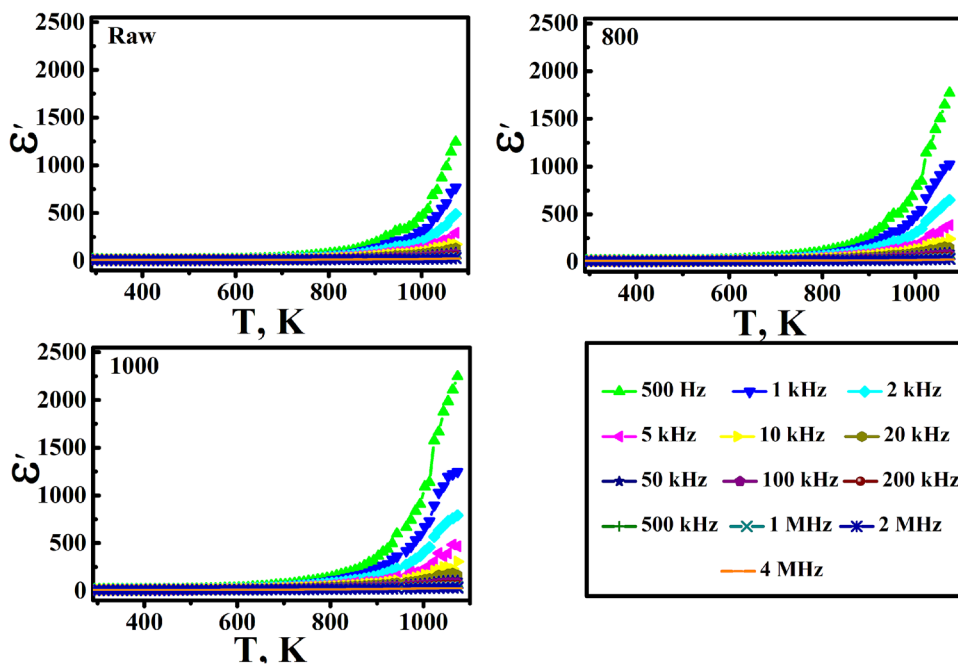
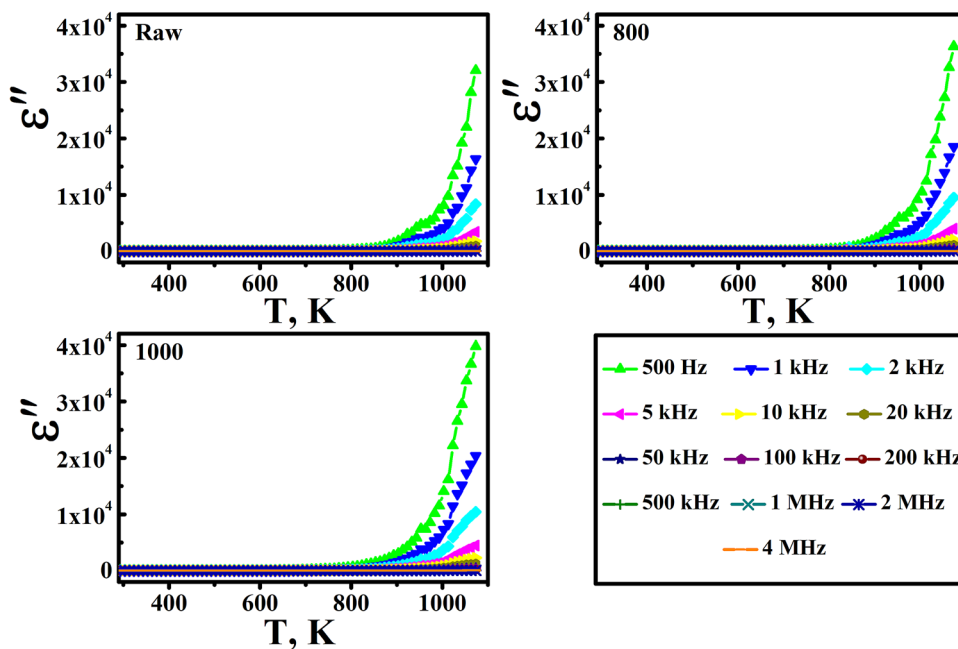


Fig. 10 Dielectric loss (ϵ'') as a function of absolute temperature at different applied frequencies for Raw, 800, and 1000 scoria samples

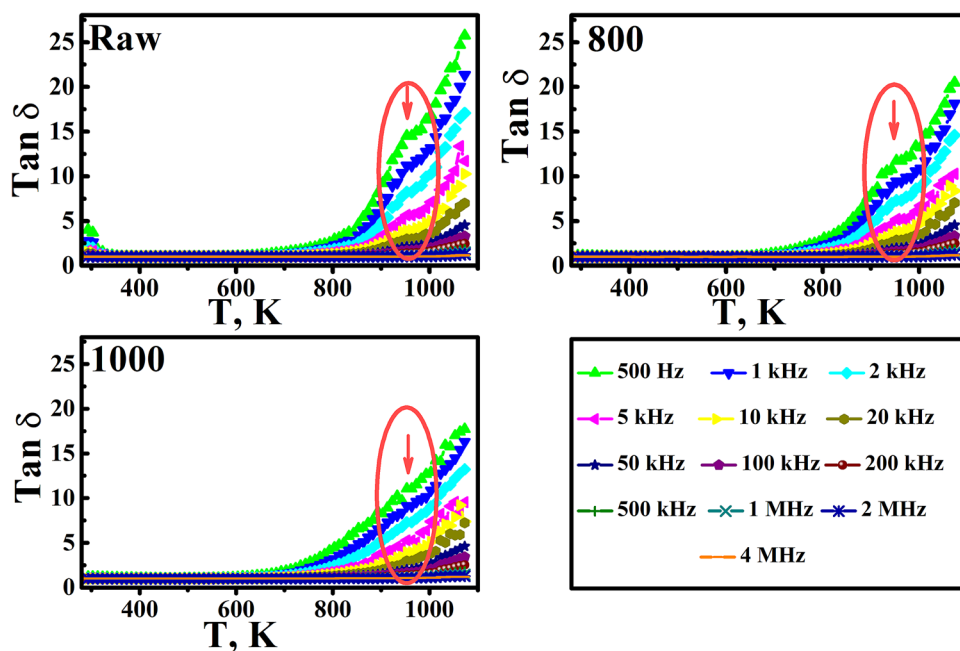


dielectric constants of 800 and 1000 scoria samples somewhat get increased, indicating the thermal treatment could enhance the polarization of scoria.

For all scoria samples, Fig. 11 displays dielectric loss tangent curves versus absolute temperatures at different applied frequencies. The curves showed stable behavior up to the temperature of 700 K, then an increase in the dielectric loss tangent with increasing temperature. However, at the higher temperature, the dielectric loss tangent decreased as frequency increased. This can be understood from the

dielectric constant that showed the same features, and it was reported [68] when the dielectric constants show an increase (the energy storage abilities increase), also dielectric losses show an increase (energy dissipations increase). From curves of dielectric loss tangent, relaxation temperature can be noticed at around of 953 K (680 °C) at all applied frequencies for only Raw and 800 scoria samples. This relaxation temperature became very weak in sample 1000. This relaxation temperature is a hematite Néel temperature [70, 71] in which the hematite goes from canted antiferromagnet

Fig. 11 Dielectric loss tangent ($\tan \delta$) as a function of absolute temperature at different applied frequencies for Raw, 800, and 1000 scoria samples



(weakly ferromagnetic) to paramagnetic phase transition. This transition appeared very weak in the 1000 scoria sample that could be because of the formation hematite–ilmenite solid solution that might affect the structural properties, as found in the results of XRD and Raman spectroscopy.

4 Conclusion

Scoria volcanic ash whose minor minerals include hematite and ilmenite has been investigated in this study. No significant changes have been detected in the structural properties of the scoria when treated with a temperature of 800 °C. However, when treating the sample to a temperature of 1000 °C, a decrease in the intensities of XRD and Raman spectrum peaks were observed, and this was attributed to the formation of the hematite–ilmenite solid solution. As for electrical measurements, all scoria samples were electrically and dielectrically stable. They showed stable and low values of conductivity and dielectric constant up to a temperature of 700 K. Therefore, it can be concluded that this type of scoria is suitable for electrical insulation applications.

Acknowledgements The authors would like to acknowledge the technical support they received from the Saudi Geological Survey, Center of Excellence in Nanotechnology at King Fahd University of Petroleum & Minerals, and Center of Nanotechnology at King Abdul Aziz University.

Compliance with ethical standards

Conflict of interest The authors declare that they have no conflict of interest.

References

- P.N. Lemougna, U.F. Chinje Melo, M.-P. Delplancke, H. Rahier, Influence of the chemical and mineralogical composition on the reactivity of volcanic ashes during alkali activation. *Ceram. Int.* **40**(1 Part A), 811–820 (2014). <https://doi.org/10.1016/j.ceramint.2013.06.072>
- D.B. Dingwell, Y. Lavallée, U. Kueppers, Volcanic ash: a primary agent in the Earth system. *Phys. Chem. Earth Parts A/B/C* **45–46**, 2–4 (2012). <https://doi.org/10.1016/j.pce.2011.07.007>
- L.N. Tchadjie, S.O. Ekolu, Enhancing the reactivity of aluminosilicate materials toward geopolymer synthesis. *J. Mater. Sci.* **53**(7), 4709–4733 (2018). <https://doi.org/10.1007/s10853-017-1907-7>
- M.F. Serra, M.S. Conconi, G. Suarez, E.F. Aglietti, N.M. Rendtorff, Volcanic ash as flux in clay based triaxial ceramic materials, effect of the firing temperature in phases and mechanical properties. *Ceram. Int.* **41**(5 Part A), 6169–6177 (2015). <https://doi.org/10.1016/j.ceramint.2014.12.123>
- Y. Zheng, S. Wang, Z. Ouyang, Y. Zou, J. Liu, C. Li, X. Li, J. Feng, CAS-1 lunar soil simulant. *Adv. Space Res.* **43**(3), 448–454 (2009). <https://doi.org/10.1016/j.asr.2008.07.006>
- H. Takeda, S. Hashimoto, H. Kanie, S. Honda, Y. Iwamoto, Fabrication and characterization of hardened bodies from Japanese volcanic ash using geopolymerization. *Ceram. Int.* **40**(3), 4071–4076 (2014). <https://doi.org/10.1016/j.ceramint.2013.08.061>
- B.I. Djon Li Ndjock, A. Elimbi, M. Cyr, Rational utilization of volcanic ashes based on factors affecting their alkaline activation. *J. Non-Cryst. Solids* **463**, 31–39 (2017). <https://doi.org/10.1016/j.jnoncrsol.2017.02.024>
- P.N. Lemougna, K-t Wang, Q. Tang, A.N. Nzeukou, N. Billong, U.C. Melo, X-m Cui, Review on the use of volcanic ashes for engineering applications. *Resour. Conserv. Recycl.* **137**, 177–190 (2018). <https://doi.org/10.1016/j.resconrec.2018.05.031>
- C. Leonelli, E. Kamseu, D.N. Boccaccini, U.C. Melo, A. Rizzuti, N. Billong, P. Miselli, Volcanic ash as alternative raw materials for traditional vitrified ceramic products. *Adv. Appl. Ceram.* **106**(3), 135–141 (2007). <https://doi.org/10.1179/174367607X159329>
- A. Husain, K. Kupwade-Patil, A.F. Al-Aibani, M.F. Abdulsalam, In situ electrochemical impedance characterization of

- cement paste with volcanic ash to examine early stage of hydration. *Constr. Build. Mater.* **133**, 107–117 (2017). <https://doi.org/10.1016/j.conbuildmat.2016.12.054>
11. K. Kupwade-Patil, A.F. Al-Aibani, M.F. Abdulsalam, C. Mao, A. Bumajdad, S.D. Palkovic, O. Büyükoztürk, Microstructure of cement paste with natural pozzolanic volcanic ash and Portland cement at different stages of curing. *Constr. Build. Mater.* **113**, 423–441 (2016). <https://doi.org/10.1016/j.conbuildmat.2016.03.084>
 12. K. Kupwade-Patil, S. Chin, J. Ilavsky, R.N. Andrews, A. Bumajdad, O. Büyükoztürk, Hydration kinetics and morphology of cement pastes with pozzolanic volcanic ash studied via synchrotron-based techniques. *J. Mater. Sci.* **53**(3), 1743–1757 (2018). <https://doi.org/10.1007/s10853-017-1659-4>
 13. E. Alemayehu, B. Lennartz, Virgin volcanic rocks: kinetics and equilibrium studies for the adsorption of cadmium from water. *J. Hazard. Mater.* **169**(1), 395–401 (2009). <https://doi.org/10.1016/j.jhazmat.2009.03.109>
 14. J. Schleppe, J. Gibbons, A. Groetsch, J. Buckman, A. Cowley, N. Bennett, Manufacture of glass and mirrors from lunar regolith simulant. *J. Mater. Sci.* **54**(5), 3726–3747 (2019). <https://doi.org/10.1007/s10853-018-3101-y>
 15. Y. Zhou, T. Wang, D. Zhi, B. Guo, Y. Zhou, J. Nie, A. Huang, Y. Yang, H. Huang, L. Luo, Applications of nanoscale zero-valent iron and its composites to the removal of antibiotics: a review. *J. Mater. Sci.* **54**(19), 12171–12188 (2019). <https://doi.org/10.1007/s10853-019-03606-5>
 16. G.K. Warati, M.M. Darwish, F.F. Feyessa, T. Ghebrab, Suitability of scoria as fine aggregate and its effect on the properties of concrete. *Sustainability* **11**(17), 4647 (2019). <https://doi.org/10.3390/su11174647>
 17. A.M. Al-Swaidani, S.D. Aliyan, Effect of adding scoria as cement replacement on durability-related properties. *Int. J. Concr. Struct. Mater.* **9**(2), 241–254 (2015). <https://doi.org/10.1007/s40069-015-0101-z>
 18. D. Bondar, C. Lynsdale, N. Milestone, N. Hassani, Sulfate resistance of alkali activated pozzolans. *Int. J. Concr. Struct. Mater.* **9**(2), 145–158 (2015). <https://doi.org/10.1007/s40069-014-0093-0>
 19. K. Ezziane, A. Bougara, A. Kadri, H. Khelafi, E. Kadri, Compressive strength of mortar containing natural pozzolan under various curing temperature. *Cem. Concr. Compos.* **29**(8), 587–593 (2007). <https://doi.org/10.1016/j.cemconcomp.2007.03.002>
 20. M. Mouli, H. Khelafi, Performance characteristics of lightweight aggregate concrete containing natural pozzolan. *Build. Environ.* **43**(1), 31–36 (2008). <https://doi.org/10.1016/j.buildenv.2006.11.038>
 21. E.F. Rajaonarison, A. Gacoin, R. Randrianja, V.G. Ranaivoniarivo, B.H.N. Razafindrabe, Effect of scoria on various specific aspects of lightweight concrete. *Int. J. Concr. Struct. Mater.* **11**(3), 541–555 (2017). <https://doi.org/10.1007/s40069-017-0204-9>
 22. Y. Ma, G. Wang, G. Ye, J. Hu, A comparative study on the pore structure of alkali-activated fly ash evaluated by mercury intrusion porosimetry, N₂ adsorption and image analysis. *J. Mater. Sci.* **53**(8), 5958–5972 (2018). <https://doi.org/10.1007/s10853-017-1965-x>
 23. X. Chen, H. Song, Y. Guo, L. Wang, F. Cheng, Converting waste coal fly ash into effective adsorbent for the removal of ammonia nitrogen in water. *J. Mater. Sci.* **53**(18), 12731–12740 (2018). <https://doi.org/10.1007/s10853-018-2394-1>
 24. H. Song, W. Xie, J. Liu, F. Cheng, K.A.M. Gasem, M. Fan, Effect of surfactants on the properties of a gas-sealing coating modified with fly ash and cement. *J. Mater. Sci.* **53**(21), 15142–15156 (2018). <https://doi.org/10.1007/s10853-018-2679-4>
 25. N. Salah, A.M. Alfawzan, A. Saeed, A. Alshahrie, W. Allafi, Effective reinforcements for thermoplastics based on carbon nanotubes of oil fly ash. *Sci. Rep.* **9**(1), 20288 (2019). <https://doi.org/10.1038/s41598-019-56777-1>
 26. C. Gunasekara, Z. Zhou, D.W. Law, M. Sofi, S. Setunge, P. Mendis, Microstructure and strength development of quaternary blend high-volume fly ash concrete. *J. Mater. Sci.* (2020). <https://doi.org/10.1007/s10853-020-04473-1>
 27. X. Zhang, W. Huo, Y. Lu, K. Gan, S. Yan, J. Liu, J. Yang, Porous Si₃N₄-based ceramics with uniform pore structure originated from single-shell hollow microspheres. *J. Mater. Sci.* **54**(6), 4484–4494 (2019). <https://doi.org/10.1007/s10853-018-3118-2>
 28. M.R. Moufti, A.A. Sabtan, O.R. El-Mahdy, W.M. Shehata, Assessment of the industrial utilization of scoria materials in central Harrat Rahat Saudi Arabia. *Eng. Geol.* **57**(3), 155–162 (2000). [https://doi.org/10.1016/S0013-7952\(00\)00024-7](https://doi.org/10.1016/S0013-7952(00)00024-7)
 29. A.A. Sabtan, W.M. Shehata, Evaluation of engineering properties of scoria in central Harrat Rahat, Saudi Arabia. *Bull. Eng. Geol. Environ.* **59**(3), 219–225 (2000). <https://doi.org/10.1007/s100640000061>
 30. M.R. Moufti, K. Németh, Harrat Rahat: the geoheritage value of the youngest long-lived volcanic field in the Kingdom of Saudi Arabia, in *Geoheritage of Volcanic Harrats in Saudi Arabia*, ed. by M.R. Moufti, K. Németh (Springer, New York, 2016), pp. 33–120
 31. N. Salah, N. Baghdadi, A. Alshahrie, A. Saeed, A.R. Ansari, A. Memic, K. Koumoto, Nanocomposites of CuO/SWCNT: promising thermoelectric materials for mid-temperature thermoelectric generators. *J. Eur. Ceram. Soc.* **39**(11), 3307–3314 (2019). <https://doi.org/10.1016/j.jeurceramsoc.2019.04.036>
 32. M.A. Gabal, W.A. Bayoumy, A. Saeed, Y.M. Al Angari, Structural and electromagnetic characterization of Cr-substituted Ni–Zn ferrites synthesized via egg-white route. *J. Mol. Struct.* **1097**, 45–51 (2015). <https://doi.org/10.1016/j.molstruc.2015.04.032>
 33. S.R. Alharbi, M. Alhassan, O. Jalled, S. Wageh, A. Saeed, Structural characterizations and electrical conduction mechanism of CaBi₂Nb₂O₉ single-phase nanocrystallites synthesized via sucrose-assisted sol–gel combustion method. *J. Mater. Sci.* **53**(16), 11584–11594 (2018). <https://doi.org/10.1007/s10853-018-2458-2>
 34. M. Akia, N. Salinas, S. Luna, E. Medina, A. Valdez, J. Lopez, J. Ayala, M. Alcoutlabi, K. Lozano, In situ synthesis of Fe₃O₄-reinforced carbon fiber composites as anodes in lithium-ion batteries. *J. Mater. Sci.* **54**(21), 13479–13490 (2019). <https://doi.org/10.1007/s10853-019-03717-z>
 35. S. Poyraz, J. Cook, Z. Liu, L. Zhang, A. Nautiyal, B. Hohmann, S. Klamt, X. Zhang, Microwave energy-based manufacturing of hollow carbon nanospheres decorated with carbon nanotubes or metal oxide nanowires. *J. Mater. Sci.* **53**(17), 12178–12189 (2018). <https://doi.org/10.1007/s10853-018-2511-1>
 36. L.G. da Trindade, G.Y. Hata, J.C. Souza, M.R.S. Soares, E.R. Leite, E.C. Pereira, E. Longo, T.M. Mazzo, Preparation and characterization of hematite nanoparticles-decorated zinc oxide particles (ZnO/Fe₂O₃) as photoelectrodes for solar cell applications. *J. Mater. Sci.* **55**(7), 2923–2936 (2020). <https://doi.org/10.1007/s10853-019-04135-x>
 37. X. Yan, Y. Wu, D. Li, J. Hu, G. Li, P. Li, H. Jiang, W. Zhang, Synthesis and evolution of α-Fe₂O₃ nanorods for enhanced visible-light-driven photocatalysis. *J. Mater. Sci.* **53**(23), 15850–15858 (2018). <https://doi.org/10.1007/s10853-018-2751-0>
 38. P. Zhang, J. Huang, Z. Shen, X. Wang, F. Luo, P. Zhang, J. Wang, S. Miao, Fired hollow clay bricks manufactured from black cotton soils and natural pozzolans in Kenya. *Constr. Build. Mater.* **141**, 435–441 (2017). <https://doi.org/10.1016/j.conbuildmat.2017.03.018>
 39. B.M. Warnes, F.F. Aplan, G. Simkovich, Electrical conductivity and seebeck voltage of Fe₂O₃, pure and doped, as a function of temperature and oxygen pressure. *Solid State Ion.* **12**, 271–276 (1984)

40. D.S. Parasnis, *Principles of Applied Geophysics* (Springer, New York, 2012)
41. M. Erdemoğlu, M. Birinci, T. Uysal, E. Porgalı Tüzer, T.S. Barry, Mechanical activation of pyrophyllite ore for aluminum extraction by acidic leaching. *J. Mater. Sci.* **53**(19), 13801–13812 (2018). <https://doi.org/10.1007/s10853-018-2606-8>
42. W. Zhu, S. Nakashima, E. Marin, H. Gu, G. Pezzotti, Microscopic mapping of dopant content and its link to the structural and thermal stability of yttria-stabilized zirconia polycrystals. *J. Mater. Sci.* **55**(2), 524–534 (2020). <https://doi.org/10.1007/s10853-019-04080-9>
43. V.K. Soni, T. Roy, S. Dhara, G. Choudhary, P.R. Sharma, R.K. Sharma, On the investigation of acid and surfactant modification of natural clay for photocatalytic water remediation. *J. Mater. Sci.* **53**(14), 10095–10110 (2018). <https://doi.org/10.1007/s10853-018-2308-2>
44. A. Bloise, Thermal behaviour of actinolite asbestos. *J. Mater. Sci.* **54**(18), 11784–11795 (2019). <https://doi.org/10.1007/s10853-019-03738-8>
45. S.A. McEnroe, P. Robinson, F. Langenhorst, C. Frandsen, M.P. Terry, T.B. Ballaran, Magnetization of exsolution intergrowths of hematite and ilmenite: Mineral chemistry, phase relations, and magnetic properties of hemo-ilmenite ores with micron- to nanometer-scale lamellae from Allard Lake, Quebec. *J. Geophys. Res.* (2007). <https://doi.org/10.1029/2007JB004973>
46. B. Burton, Thermodynamic analysis of the system Fe₂O₃-FeTiO₃. *Phys. Chem. Miner.* **11**(3), 132–139 (1984). <https://doi.org/10.1007/BF00309251>
47. G. Li, G. Zheng, Z. Ding, L. Shi, J. Li, Z. Chen, L. Wang, A.A.O. Tay, W. Zhu, High-performance ultra-low-k fluorine-doped nanoporous organosilica films for inter-layer dielectric. *J. Mater. Sci.* **54**(3), 2379–2391 (2019). <https://doi.org/10.1007/s10853-018-3013-x>
48. Y. Peng, N. Pan, D. Wang, J. Yang, Z. Guo, W. Yuan, A Si–O–Si bridge assembled from 3-mercaptopropyltrimethoxysilane and silicon carbide for effective charge transfer in photocatalysis. *J. Mater. Sci.* **53**(17), 12432–12440 (2018). <https://doi.org/10.1007/s10853-018-2518-7>
49. B.B. Kenne Dikko, A. Elimbi, M. Cyr, J. Dika Manga, H. Tchakoute Kouamo, Effect of the rate of calcination of kaolin on the properties of metakaolin-based geopolymers. *J. Asian Ceram. Soc.* **3**(1), 130–138 (2015). <https://doi.org/10.1016/j.jascer.2014.12.003>
50. P. Krolop, A. Jantschke, S. Gilbricht, K. Niiranen, T. Seifert, Mineralogical imaging for characterization of the per Geijer Apatite iron ores in the Kiruna District, Northern Sweden: a comparative study of mineral liberation analysis and Raman imaging. *Minerals* **9**(9), 544 (2019). <https://doi.org/10.3390/min9090544>
51. M.L. Frezzotti, F. Tecce, A. Casagli, Raman spectroscopy for fluid inclusion analysis. *J. Geochem. Explor.* **112**, 1–20 (2012). <https://doi.org/10.1016/j.gexplo.2011.09.009>
52. F. Rull, J. Martínez-Frias, J.A. Rodríguez-Losada, Micro-Raman spectroscopic study of El Gasco pumice, western Spain. *J. Raman Spectrosc.* **38**(2), 239–244 (2007). <https://doi.org/10.1002/jrs.1628>
53. J. Hövelmann, A. Putnis, T. Geisler, B.C. Schmidt, U. Gollaschindler, The replacement of plagioclase feldspars by albite: observations from hydrothermal experiments. *Contrib. Miner. Petrol.* **159**(1), 43–59 (2010). <https://doi.org/10.1007/s00410-009-0415-4>
54. S.S. Palinkaš, R. Wegner, A. Čobić, L.A. Palinkaš, B.S. De Brito, T. Váczi, V. Bermanec, The role of magmatic and hydrothermal processes in the evolution of Be-bearing pegmatites: evidence from beryl and its breakdown products. *Am. Miner.* **99**(2–3), 424–432 (2014). <https://doi.org/10.2138/am.2014.4500>
55. A. Kumar, S. Sarmah, AC conductivity and dielectric spectroscopic studies of polypyrrole–titanium dioxide hybrid nanocomposites. *Phys Status Solidi (A)* **208**(9), 2203–2210 (2011). <https://doi.org/10.1002/pssa.201026721>
56. C.T. de Almeida e Silva, V. Fernandes Kettermann, C. Pereira, M. Simões, M. Wilhelm, K. Rezwani, Novel tape-cast SiOC-based porous ceramic electrode materials for potential application in bioelectrochemical systems. *J. Mater. Sci.* **54**(8), 6471–6487 (2019). <https://doi.org/10.1007/s10853-018-03309-3>
57. M.A. Gabal, F. Al-Solami, Y.M. Al Angari, A. Awad, A.A. Al-Juaid, A. Saeed, Structural, magnetic, and electrical characterization of Sr-substituted LaFeO₃ perovskite synthesized via sucrose auto-combustion route. *J. Mater. Sci.* **31**(4), 3146–3158 (2020). <https://doi.org/10.1007/s10854-020-02861-6>
58. C.O. Park, S.A. Akbar, Ceramics for chemical sensing. *J. Mater. Sci.* **38**(23), 4611–4637 (2003). <https://doi.org/10.1023/A:1027402430153>
59. W. Pan, M. Cao, C. Diao, C. Tao, H. Hao, Z. Yao, Z. Yu, H. Liu, Structures and dielectric properties of (Nb, Zn) co-doped SrTiO₃ ceramics at various sintering temperatures. *J. Mater. Sci.* **54**(19), 12401–12410 (2019). <https://doi.org/10.1007/s10853-019-03793-1>
60. A.A. Pritam, A.L. Sharma, Dielectric relaxations and transport properties parameter analysis of novel blended solid polymer electrolyte for sodium-ion rechargeable batteries. *J. Mater. Sci.* **54**(9), 7131–7155 (2019). <https://doi.org/10.1007/s10853-019-03381-3>
61. J. Exner, J. Kita, R. Moos, In- and through-plane conductivity of 8YSZ films produced at room temperature by aerosol deposition. *J. Mater. Sci.* **54**(21), 13619–13634 (2019). <https://doi.org/10.1007/s10853-019-03844-7>
62. M.A. Gabal, A.A. Al-Juaid, S. El-Rashed, M.A. Hussein, Y.M. Al Angari, A. Saeed, Structural, thermal, magnetic and electrical properties of polyaniline/CoFe₂O₄ nano-composites with special reference to the dye removal capability. *J. Inorg. Organomet. Polym. Mater.* **29**(6), 2197–2213 (2019). <https://doi.org/10.1007/s10904-019-01179-z>
63. M.A. Gabal, N.H. Al-Zahrani, Y.M.A. Angari, A. Saeed, Substitution effect on the structural, magnetic, and electrical properties of Co_{1-x}Zn_xFe₂O₄ nanocrystalline ferrites (x = 0–1) prepared via gelatin auto-combustion method. *IEEE Trans. Magn.* **54**(1), 1–12 (2018). <https://doi.org/10.1109/TMAG.2017.2752726>
64. J. Shanker, M.B. Suresh, G.N. Rao, D.S. Babu, Colossal dielectric, relaxor ferroelectric, diamagnetic and weak ferromagnetic properties of NdCrO₃ perovskite nanoparticles. *J. Mater. Sci.* **54**(7), 5595–5604 (2019). <https://doi.org/10.1007/s10853-018-03226-5>
65. R. Verma, S.P. Tiwari, R. Kumari, R. Srivastava, Study of enhancement in the dielectric and electrical properties of WO₃-doped LiF nano-composite. *J. Mater. Sci.* **53**(6), 4199–4208 (2018). <https://doi.org/10.1007/s10853-017-1870-3>
66. J. Sun, R. Ahmed, G.J. Wang, S.T. Wang, J. Wang, S.A. Suhaib, Y.M. Xie, H. Bi, C.C. Wang, Colossal dielectric behavior and dielectric anomalies in Sr₂TiCrO₆ ceramics. *J. Mater. Sci.* **54**(8), 6323–6331 (2019). <https://doi.org/10.1007/s10853-018-03298-3>
67. M.K. Vyas, A. Chandra, Synergistic effect of conducting and insulating fillers in polymer nanocomposite films for attenuation of X-band. *J. Mater. Sci.* **54**(2), 1304–1325 (2019). <https://doi.org/10.1007/s10853-018-2894-z>
68. F. Oliveira, N. Dencheva, P. Martins, S. Lanceros-Méndez, Z. Denchev, A new approach for preparation of metal-containing polyamide/carbon textile laminate composites with tunable electrical conductivity. *J. Mater. Sci.* **53**(16), 11444–11459 (2018). <https://doi.org/10.1007/s10853-018-2435-9>
69. S.M. Salem, E.M. Antar, A.G. Mostafa, S.M. Salem, S.A. Elbadry, Compositional dependence of the structural and dielectric properties of Li₂O–GeO₂–ZnO–Bi₂O₃–Fe₂O₃ glasses. *J. Mater.*

- Sci. **46**(5), 1295–1304 (2011). <https://doi.org/10.1007/s10853-010-4915-4>
70. J.-F. Lin, W. Sturhahn, J. Zhao, G. Shen, H-k Mao, R.J. Hemley, Chapter 19 - Nuclear resonant inelastic X-ray scattering and synchrotron Mössbauer spectroscopy with laser-heated diamond anvil cells, in *Advances in High-Pressure Technology for Geophysical Applications*, ed. by J. Chen, Y. Wang, T.S. Duffy, G. Shen, L.F. Dobrzhinetskaya (Elsevier, Amsterdam, 2005), pp. 397–411
71. E. Brok, C. Frandsen, K. Lefmann, S. McEnroe, P. Robinson, B.P. Burton, T.C. Hansen, R. Harrison, Spin orientation in solid solution hematite-ilmenite. *Am. Miner.* **102**(6), 1234–1243 (2017). <https://doi.org/10.2138/am-2017-5792CCBY>

Publisher's Note Springer Nature remains neutral with regard to jurisdictional claims in published maps and institutional affiliations.